Sensors and Actuators: A. Physical 335 (2022) 113398

Contents lists available at ScienceDirect

Sensors and Actuators: A. Physical

journal homepage: www.elsevier.com/locate/sna

An interferometric inertial sensor for low-frequency seismic isolation

Binlei Ding[a,b], Guoying Zhao[c,*], Jennifer Watchi[a], Ameer Sider[d], Christophe Collette[a,d]

[a] Precision Mechatronics Laboratory, Université Libre de Bruxelles, Belgium
[b] Auto Product Strategy & New Technology Research Institute, BYD Auto Industry Company Limited, China
[c] MOE Key Laboratory of TianQin Mission, TianQin Research Center for Gravitational Physics & School of Physics and Astronomy, Frontiers Science Center for TianQin, CNSA Research Center for Gravitational Waves, Sun Yat-sen University, China
[d] Precision Mechatronics Laboratory, Université de Liège, Belgium

ARTICLE INFO

Article history:
Received 28 June 2021
Received in revised form 21 November 2021
Accepted 20 January 2022
Available online 22 January 2022

Keywords:
Interferometric readout
Lehman pendulum
Inertial sensor

ABSTRACT

In this paper, a high-resolution Horizontal Interferometric Inertial Sensor (HINS) is developed for active seismic isolation of gravitational wave detection instrument. Its resonance frequency can be tuned down to as low as 0.08 Hz thanks to the use of a Lehman pendulum and the inverted pendulum like mechanisms. Combined with a novel homodyne quadrature interferometer, a high resolution of 2×10^{-13} m/$\sqrt{\text{Hz}}$ (or 7.9×10^{-12} (m/s^2)/$\sqrt{\text{Hz}}$) at 1 Hz can be obtained. A dynamic analysis is performed to investigate the response of the HINS to different types of excitations. A noise budgeting of the HINS is also conducted, which indicates that the resolution of HINS is limited by the thermomechancial noise from 0.01 to 1 Hz and by the thermal electrical noise of the photodetectors above 1 Hz.

1. Introduction

Seismic activities happen all the time and everywhere. Even through they are hard to feel, they do adversely influence the functionalities of large ground-based instrument. For example, seismic noise has to be well-isolated for the Advanced Laser Interferometer Gravitational-wave Observatory (aLIGO) [1], and the Compact Linear Collider (CLIC) [2].

Amongst different strategies of instrument stabilisation, the inertial feedback control shows the advantage to mitigate the transmission of seismic motion at low frequencies (say, below 1 Hz) [3]. High-resolution inertial sensors are required to improve the performance of the strategy [4]. Take the example of aLIGO, different inertial sensors are applied in the isolation system [5], and their resolutions were experimentally assessed in [6]. Amongst the sensors, the resolution of Geotech GS-13 [7] is 8×10^{-12} m/$\sqrt{\text{Hz}}$ at 1 Hz. However, inertial sensors with higher resolutions at low frequencies are particularly preferred in order to further improve the seismic isolation [8].

Generally, there are two main methods to improve the resolution of an inertial sensor. The first one is to decrease the noise floor of its readout. Compared to capacitive or eddy current readouts, interferometric readouts exhibit advantages in terms of noise and dynamic range [9,10]. Several developments on replacing the original readouts of commercial sensors by interferometric readouts were conducted by [11–13] and combining home-made mechanics with interferometric readouts were conducted by [14,15]. The second method is to lower the resonance frequency of the mechanics. This can be done, for example, by using the Lacoste pendulum [14] (7 Hz)[1] and the Geometric Anti-Springs (GAS) mechanics [16] (1 Hz) for the vertical measurement, and the parallelogram mechanics [17] (2.2 Hz) and the folded pendulum [18] (0.54 Hz) for the horizontal measurement. Among these, the folded pendulums were extensively studied for implementing horizontal seismometers thanks to its capability of reducing the resonance frequency [18–21]. Barone *et al.* [20] reported that the resonance frequency can reach 0.06 Hz. However, these prototypes are monolithic mechanics with notched hinges, so they are not easy to manufacture. Alternatively, Lehman pendulum is another well-known mechanics used in horizontal seismometers such as the STS-1 seismometers [22].

A novel inertial sensor, HINS, is proposed in this paper. The goal of the paper is to provide a critical analysis of the dynamics and the noise budgeting of the proposed sensor. Section 2 presents the dynamic analysis of the mechanics, the working principle of the interferometric readout and the data processing. The experimental assessments are given in Section 3. Section 4 presents the noise budgeting of the sensor. Section 5 draws the conclusions.

* Corresponding author.
E-mail address: zhaoguoying@mail.sysu.edu.cn (G. Zhao).

[1] the value is the resonance frequency of the mechanics

https://doi.org/10.1016/j.sna.2022.113398
0924-4247/

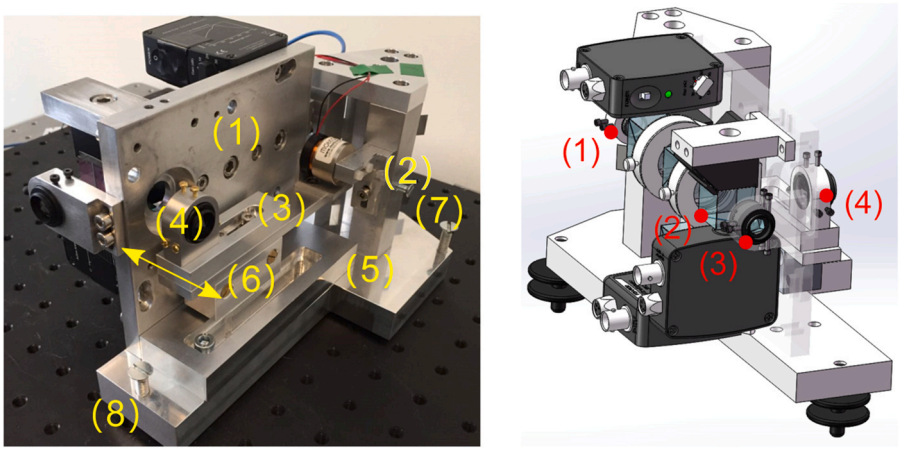

Fig. 1. (a) Prototype of HINS, the arrow shows the oscillation direction: (1) interferometric readout, (2) joint, (3) horizontal pendulum, (4) corner cube, (5) base, (6) proof-mass, (7 &8) screws; (b) Optical path in HINS: The red points with numbers show the optical path from the laser collimator (1) to the polarising beam splitter (2), and to the fixed corner cube (3) and movable corner cube (4). The details of the optical path is presented by Fig. 7.

2. Description of HINS

Fig. 1 a shows the developed prototype of HINS. The dimension of the sensor is about $220 \times 160 \times 140\ mm^3$ (length × width × height). The sensor consists of two parts, the mechanics and the interferometric readout (1, see Fig. 7a). The joint (2) is a pair of home-made cross-spring hinges (see Fig. 2), which defines the rotation axis of the horizontal pendulum (3). A retro-reflector (corner cube (4)) is mounted at the end of the pendulum, and forms the measuring arm of the interferometric readout (1). A proof-mass (6) is mounted at the free end of the pendulum where two screws are also attached to adjust the centre of mass and the inertia of the pendulum. Three screws (7 and 8, the third one is on the back) on the base (5) are used to adjust the tilting angle between the base and the horizontal ground. Fig. 1b shows the Computer-Aided Design (CAD) model of the prototype. Some components are transparently shown to display the optical path. The laser beam passes through the collimator (1) and the polarising beam splitter (2). this splitter separates the beam into the reference arm with the fixed corner cube (3), and into the measurement arm with the movable corner cube (4). Consequently, the motion of the pendulum can be measured by the interferometric readout.

Fig. 2a shows a cross-spring hinge. It consists of two supports (1), four spring-holders (2) and two strips (300 series stainless steel) (3). The length of one strip is around 50 mm, and the effective length is $l = 6$ mm after being clamped by the supports and strip-holders. Its width and thickness are $w = 12.5$ mm and $t = 0.038$ mm. The two supports are the same, but they have a 2 mm height shift in the assembly. Fig. 2b shows a sketch of the top view of a cross-spring hinge with pendulum. The lower holder is fixed on the frame and the upper one is mounted with the pendulum (4) and rotates around the crossing point of the strips (3). The rotational stiffness in the presence of axial load (with the rotational motion is less than 15°), can be estimated as [23].

$$k = \frac{2Ewt^3}{3l}(3c^2 - 3c + 1) + []\frac{2(9c^2 - 9c + 1)}{15\cos(\frac{\alpha}{2})} + c\cos(\frac{\alpha}{2})]Pl \quad (1)$$

where $E = 200$ Gpa is the Young's modulus of the material, $\alpha = \pi/2$ rad is the crossing angle of two strips. $c = 1/2$ is geometric parameter indicating the crossing position of the strips at the midpoint. P is the axial load along the pendulum, and it equals to 0 when the pendulum is horizontally oriented. Fig. 2c presents the final assembled hinges which are vertically mounted with the mechanics.

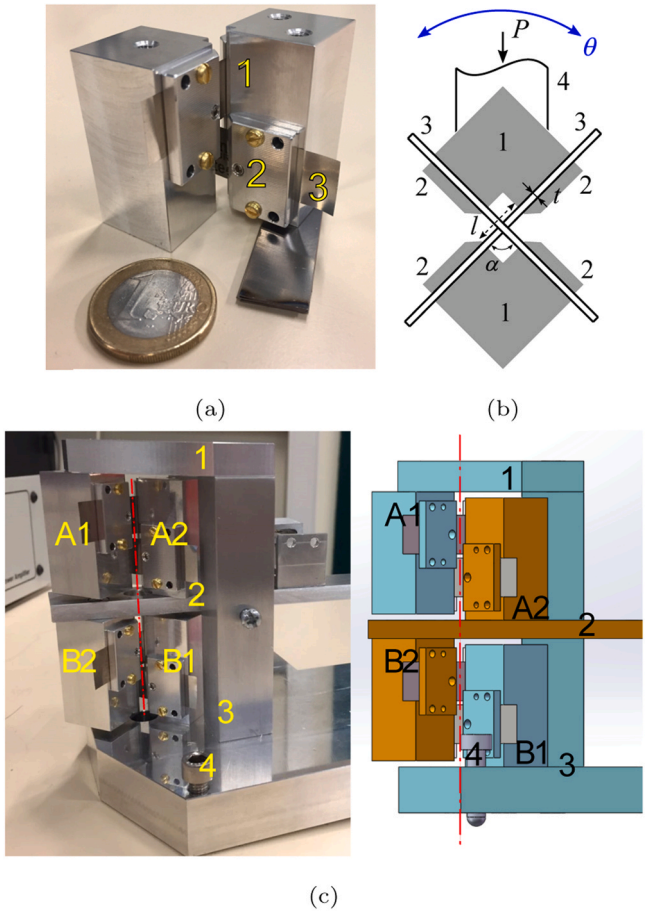

Fig. 2. Joints of HINS: (a) One hinge used in HINS: 1 support, 2 strip-holder, 3 stainless steel strip; (b) Top view of the hinge: 4 pendulum, P is the axial load along the pendulum, θ is the rotational motion of the pendulum; (c) Two hinges assembled as the joint of HINS: 1 support, 2 pendulum, 3 base, 4 screws, A1&A2 and B1&B2 are two pairs of supports, A1&B1 are mounted on the base (in cyan), A2&B2 are mounted on the pendulum (in orange). Dash-dot red line: rotational axis of the pendulum.

The supports (A1, B1) of the two crossed-spring hinges are fixed on the stable frame (1) and the base (3) of the mechanics. The supports (A2, B2) rotate together with the pendulum (2). The dash-dot line indicates the rotation axis of the pendulum. Therefore, a simplified

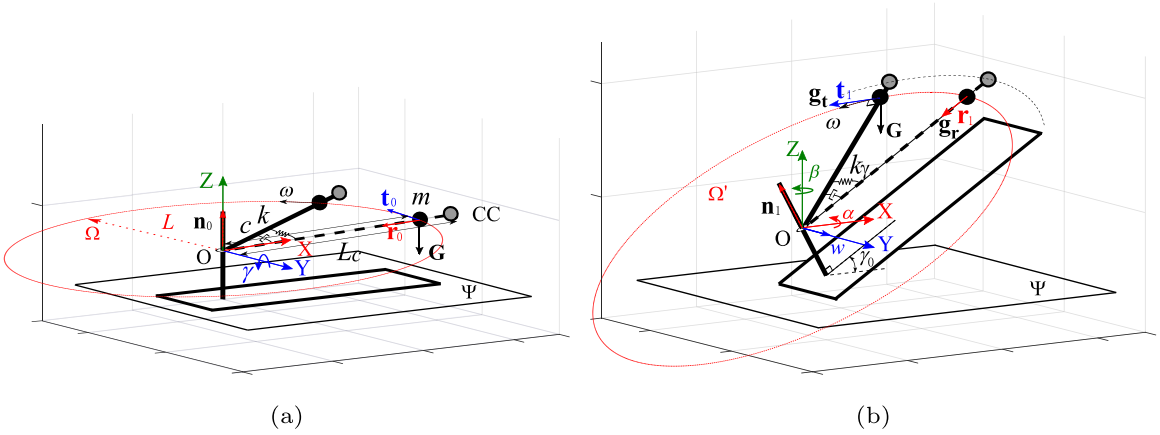

Fig. 3. The model of the Lehman pendulum: (a) The model without tilting, the proof-mass rotates in the Ω plane; (b) The model with the tilting γ_0 about Y-axis, the proof-mass rotates in the Ω′ plane. The joint O presents the cross-spring hinge allowing oscillations. Black dots present the mass centre of the pendulum, and grey dots present the mounting of the corner cube. The dashed line denotes the initial position of the pendulum. The translation w along Y-axis as well as rotational motions $\boldsymbol{\alpha}$, $\boldsymbol{\gamma}$ and $\boldsymbol{\beta}$ about X-axis, Y-axis and Z-axis of the frame can be defined on the point O.

estimation of the joint stiffness is given by summing stiffness k with axial load $P = mg\cdot\sin(\gamma_0)/2$, where m = 0.5 kg is the mass of the pendulum and γ_0 is the tilting angle of the mechanics. Assuming the tilting angle γ_0 = 0.5°, the estimation of the joint stiffness $k_\gamma = 2k$ equals to 0.0086 Nm/rad.

2.1. Mechanics

The resonance frequency of the garden-gate pendulum (Lehman pendulum) without considering the joint stiffness can be preliminarily estimated by Wielandt [24]. In order to better study the dynamics of the pendulum, the stiffness of the hinge is considered. Fig. 3 presents the model of the mechanics. Ψ is a reference plane referring to the ground, which is perpendicular to gravity. O refers to the rotational centre of the pendulum which is the origin of a Cartesian coordinate system. X-axis defines the direction of the initial position of the pendulum (dash line); Z-axis defines the opposite direction of gravity. When the pendulum rotates around the point O, the rotation occurs in the Ω plane as indicated by the red circle. Note that the rotation range of the pendulum is small in practice. It is assumed that the proof-mass m only oscillates in the Ω plane, ω denotes the rotation of the pendulum with a damping coefficient c and stiffness k. The length between the corner cube and the rotational centre is L_c and the length between the mass centre and the rotational centre is L. The vector $G = [0,\ 0,\ -mg]^\top$ represents the gravitational force at the centre of the mass.

Fig. 3b represents the scenario when the mechanics is tilted. The vector $\mathbf{g_r}$ points to the rotation point in the Ω′ plane and its magnitude $g_r = mg\sin(\gamma_0)$ is the axial load applied on the joint. According to Eq. (1), the rotational stiffness of the joint can be estimated, and it is denoted by k_γ. The variation of the stiffness k_γ during oscillation is not addressed in the following discussion. The motion of the proof-mass causes the variation of potential energy. Therefore, the contribution of the gravitational force is taken into account. $\mathbf{g_t}$ is the component of the gravitational force in the Ω′ plane and its magnitude is

$$g_t = mg\sin(\gamma_0)\sin(\omega) \tag{2}$$

where ω is the rotation of the proof-mass, and the expression of g_t is derived in Appendix.

Moreover, three excitations cause the rotation of the proof-mass about the point O. They are the translational motion w along Y-axis, rotational motion β about Z-axis and rotational motion α about X-axis. As the rotation of the proof-mass can be studied in the Ω′ plane, Fig. 4 shows the motion of the proof-mass under different excitations in the Ω′ plane.

2.1.1. Response to translational motion w

Even through the pendulum is tilted about Y-axis in Fig. 4a, the projection of the translational motion w is the same in the Ω′ plane. As shown in Fig. 3b, the rotation of the proof-mass ω equals to the relative motion θ between the frame and the pendulum. Applying Newton's second law of rotation about the hinge O in the Ω′ plane, the sum of torque about the hinge O is given by

$$I\ddot{\theta} = \sum \tau = -\tau_s - \tau_d + m\ddot{w}L\cos(\theta) + g_t L \tag{3}$$

where I is the moment of inertia with respect to the rotation centre O, $\tau_s = k_\gamma\theta$ is the rotational spring torque, $\tau_d = c\dot{\theta}$ is the rotational damping torque, $m\ddot{w}$ is the reaction force on the centre of mass and $g_t L$ is contributed by the gravitational force.

As the relative angle θ is relative small, the approximation $\sin(\theta) \approx \theta$ is applied. The interferometric readout measures this relative motion y by

$$y = -\sin(\theta)L_c = -\theta L_c \tag{4}$$

Therefore, its dynamic equation is

$$I\ddot{y} + c\dot{y} + ()k_\gamma - mg\sin(\gamma_0)L\,)y = -m\ddot{w}LL_c \tag{5}$$

Using the Laplace transformation, Eq. (5) becomes

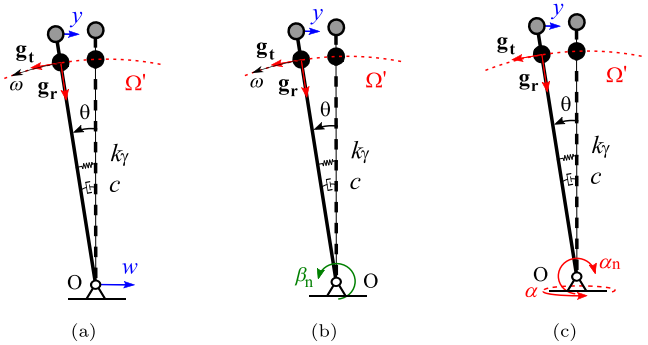

Fig. 4. Motion of the proof-mass under different excitations: the unmarked geometric parameters are defined in Fig. 3. θ is the relative rotation between the pendulum and the frame. (a) the proof-mass is excited by w in the Ω′ plane; (b) the proof-mass is excited by $\boldsymbol{\beta}$: β_n is the projection of $\boldsymbol{\beta}$ in the Ω′ plane; (c) the whole mechanics tilting by the angle α. Because the pendulum is tilted, the proof-mass is excited by $\boldsymbol{\alpha}$: α_n is the projection of $\boldsymbol{\alpha}$ in the Ω′ plane.

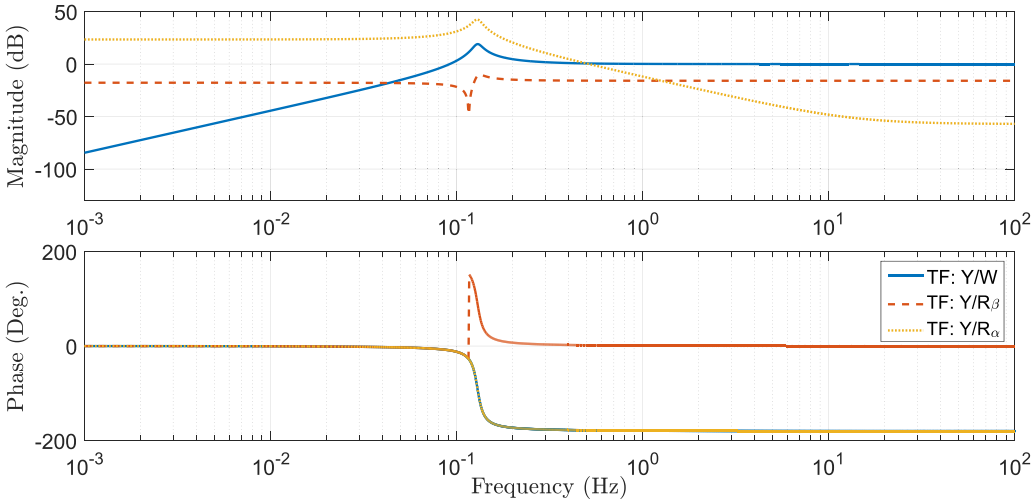

Fig. 5. Frequency response of the transfer functions of the HINS: solid blue curve: TF between Y and W, dash red curve: TF between Y and R_β, dotted yellow curve: TF between Y and R_α. For plotting the curve, tilting angle: $\gamma_0 = 0.5^\circ$, proof-mass: $m = 0.5$ kg, pendulum length and frame length: $L = L_c = 0.18$ m, inertia of the pendulum: $I = mL^2 = 0.0162$ kgm^2. According to Eq. (1), the stiffness of the joint is assumed as $k_\gamma = 0.0086$ Nm/rad and the damping coefficient is assumed as $c = 0.0015$ Nm · s/rad.

$$T_{WY} = \frac{Y(s)}{W(s)} = \frac{-mLL_c s^2}{Is^2 + cs + ()k_\gamma - mg\sin(\gamma_0)L)} \tag{6}$$

where T_{WY} is the transmissibility of the HINS to the translational excitation W.

2.1.2. Response to rotational motion β

As shown in Fig. 4b, applying Newton's second law of rotation about the hinge O in the Ω' plane, the sum of torque about the hinge O is given by

$$I\ddot{\theta} = \sum \tau = -\tau_s - \tau_d - I\ddot{\beta}_n + g_t L \tag{7}$$

where $\tau_s = k_\gamma\theta$ is the torque generated by the rotational spring, $\tau_d = c\dot{\theta}$ is the rotational damping torque, $I\ddot{\beta}_n$ is the reaction torque and $g_t L$ is the contribution of the gravitational force. The derivations of β_n and g_t are given in Appendix. Combining Eq. (4), the dynamic equation of the mechanics under this rotational excitation can be derived by

$$I\ddot{y} + c\dot{y} + ()k_\gamma - mgL\sin(\gamma_0))y = L_c\cos(\gamma_0)()I\ddot{\beta} + mgL\sin(\gamma_0)\beta) \tag{8}$$

where approximations $\sin(\theta) \approx \theta$ and $\sin()\theta - \beta\cos(\gamma_0)) \approx \theta - \beta\cos(\gamma_0)$ are applied. Using the Laplace transform, Eq. (8) becomes

$$T_{R\beta}Y = \frac{Y(s)}{R_\beta(s)} = \frac{L_c\cos(\gamma_0)()Is^2 + mgL\sin(\gamma_0))}{Is^2 + cs + ()k_\gamma - mgL\sin(\gamma_0))} \tag{9}$$

where R_β is rotation β in the Laplace domain, $T_{R\beta}Y$ is the transmissibility of the HINS to the rotational motion R_β.

2.1.3. Response to rotational motion α

As shown in Fig. 4c, applying the Newton's second law of rotation about the hinge O in the Ω' plane, the sum of torque about the hinge O is given by

$$I\ddot{\theta} = \sum \tau = -\tau_s - \tau_d + I\ddot{\alpha_n} + g_t L \tag{10}$$

where the derivations of α_n and g_t are given in Appendix.

Applying approximations $\sin(\theta) \approx \theta$, $\cos(\theta) \approx 1$, $\sin(\alpha\sin(\gamma_0)) \approx \alpha\sin(\gamma_0)$ and $\cos(\alpha\sin(\gamma_0)) \approx 1$, Eq. (10) is simplified to

$$I\ddot{\theta} = -c\dot{\theta} - k_\gamma\theta + I\ddot{\alpha}\sin(\gamma_0) + mgL\cdot()\theta\sin(\gamma_0) + \alpha\sin^2(\gamma_0) - \alpha\cos(\gamma_0) + \theta\alpha^2\cos(\gamma_0)\sin(\gamma_0)) \tag{11}$$

where the items $\alpha\sin^2(\gamma_0)$ and $\theta\alpha^2\cos(\gamma_0)\sin(\gamma_0)$ are neglected considering the 2^{nd} order small quantities. Substituting Eq. (4) into (11), it yields

$$T_{R\alpha}Y = \frac{Y(s)}{R_\alpha(s)} = \frac{-L_c\sin(\gamma_0)Is^2 + mgLL_c\cos(\gamma_0)}{Is^2 + cs + ()k_\gamma - mgL\sin(\gamma_0))} \tag{12}$$

where R_α is Laplace transform of α. $T_{R\alpha}Y$ is the transmissibility of the HINS to the rotational motion R_α.

Fig. 5 shows the frequency response function of Eqs. (6), (9) and (12). The transfer function T_{WY} (solid blue curve) shows that the HINS is a perfect estimator for displacement w above the resonance frequency around 0.12 Hz because of its flat transfer function. However, the transfer functions $T_{R\beta}Y$ (dash red curve) and $T_{R\alpha}Y$ (dotted yellow curve) show that the HINS is also the estimator of rotational motions β or α. Concerning the transfer function $T_{R\beta}Y$, the magnitude of the flat transfer function above its resonance is scaled by the factor of $L_c\cos(\gamma_0)$ in Eq. (9). Also, the transfer functions $T_{R\beta}Y$ has zeros due to the gravitational force. The type of zeros (real or conjugate complex zeros) depends on the tilting direction, and the position depends on the tilting angle γ_0. When the angle γ_0 is tuned to 0, the position of the zeros moves to a lower frequency, and the magnitude of the flat transfer function below the zeros decreases in the situation. Compared with the transfer functions T_{WY} and $T_{R\beta}Y$, it shows that depending on the amplitude of the excitations, the measurement of the HINS can be dominated by the rotational motion β below 0.04 Hz. The transfer function $T_{R\alpha}Y$ has zeros as well, the type of zeros (real or conjugate complex zeros) depends on the tilting direction, and the position depends on the tilting angle γ_0. The magnitude of the flat transfer function below its resonance increases while the frequency of the resonance decreases. It shows that depending on the amplitude of the excitations, the HINS tends to act as a tilt-meter in low frequencies below 0.5 Hz. Therefore, care has to be given when interpreting the response of the HINS at low frequency which is actually determined by both tilting and translational excitations.

2.1.4. Adjustment of resonance frequency

According to the dynamic equations of the mechanics, the resonance frequency f_0 can be simplified to

$$f_0 = \frac{1}{2\pi}\sqrt{\frac{k_\gamma - mg\sin(\gamma_0)L}{I}} \tag{13}$$

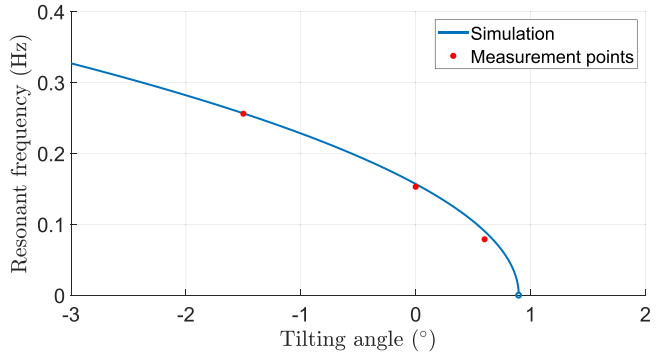

Fig. 6. The effect of tilting angle to the resonance frequency of the structure. A negative sign indicates the pendulum towards to the ground. The measurements points are presented in Section 3.

Eq. (13) shows that the resonance frequency of the pendulum is tunable by adjusting the inertial moment of the pendulum and the tilting angle. Fig. 6 indicates the resonance frequency of the structure with respect to the tilting angle. The inertial moment is simplified to $I = mL^2$ in Eq. (13). The geometries of the hinge are given in Eq. (1).

When $\gamma_0 = 0$, the mechanics is horizontally positioned, the resonance frequency equals to 0.15 Hz. When $\gamma_0 < 0$, the resonance frequency increases because of the additional restoring force contributed by the gravity. When $\gamma_0 > 0$, as suggested by the configuration in Fig. 3b, the effect of gravity comes to reduce the original restoring force, thus resonance frequency is decreased. However, when $\gamma_0 > \arcsin(\frac{k_\gamma}{mgL})$, HINS becomes unstable. Therefore, choosing the tilting angle of the mechanics is a trade-off between the low resonance frequency and the stability.

2.2. Interferometric readout

Fig. 7 exhibits the prototype of the interferometric readout under development. The dimension of the prototype is 140 × 100 mm^2. The laser source (*Koheras X15*) generates a linearly polarised laser beam, whose wavelength and beam intensity are 1550 nm and 4 mW. This laser beam passes through the polarisation-maintaining fibre of the laser source and is collimated by the collimator (*F240APC*). The beam diameter of the laser is 1.6 mm. The optical components include three polarising beamsplitter cubes (PBS1&2&3, *PBS204*), two corner cubes (CC1&2, *PS974M-C*), one non-polarising beamsplitter cube (BS, *BS018*), one quarter-wave plate (WPQ, *WPQ10E*) and one half-wave plate (WPH, *WPH10E*). The photodetectors in the setup are three switchable gain amplified photodiodes(PD1&2&3, *PDA50B2*). The gain of the photodetectors is 20 dB.

The working principle of the interferometric readout is based on the homodyne quadrature interferometer. Solid red lines with arrows in Fig. 7 show the propagation of a single laser beam with different polarisation states. The orientation of the laser collimator makes a linear polarisation near to the p-polarisation and PBS1 works as a filter to ensure the p-polarised transmitted beam. The angle between the fast axis of WPQ and the s-polarisation of laser beam is 45°. Therefore, the linear polarisation of the beam changes to the circular one after passing WPQ. Then, half energy of a beam transmits from BS and the other half is lost. The angle between the fast axis of WPH and the s-polarisation is 22.5°. Because of WPH, the two orthogonal states rotate about the propagation direction with 45°, and now can be regarded as one p-polarisation state and a s-polarisation with a phase delay of $\pi/2$ rad. At PBS2, these two polarisation states separate with each other, and dotted red line and dash red line respectively shows the propagation in the measurement arm and reference arm.

In the measurement arm, a beam with s-polarisation goes to CC1, which mounts on the mechanics of the inertial sensor. In the reference arm, a beam with p-polarisation goes to fixed CC2. Ignoring the undesirable polarisation change in corner cubes [25], the two reflected beams combine again at PBS2, which can be regarded as two beams with p- and s-polarisation states. They do not interfere because of their different polarisation. Purple lines with arrows represent the two co-propagating beams. During the propagation, WPH rotates these two linear polarisation states with the same angle of $\pi/4$ rad. BS divides the beams into two directions. About transmitted beams, the current orientation of WPQ introduces no polarisation change. At PBS1, the component with s-polarisation states in the co-propagating beams interfere with each other and measured by PD1. Blue lines with arrows show the interferometric beam. About reflected beams from BS, the components with s-polarisation states of the two beams interfere with each on the reflection way of PBS3 and components with p-polarisation states interfere on the transmission way. PD2 and PD3 respectively measure the interferometric beam with s-polarisation and p-polarisation.

2.3. Acquisition and processing

The homodyne quadrature interferometer allows to extend the measurement range of the interferometer [10]. As shown in Fig. 7, the displacement of CC1, y, introduces an optical path difference and is covered into the phase variation by [26].

$$\phi_y = \frac{2\pi n y}{\lambda} \tag{14}$$

where ϕ_y is the phase variation in terms of the optical path difference, $n \simeq 1$ is the refractive index of the optical path, λ is the

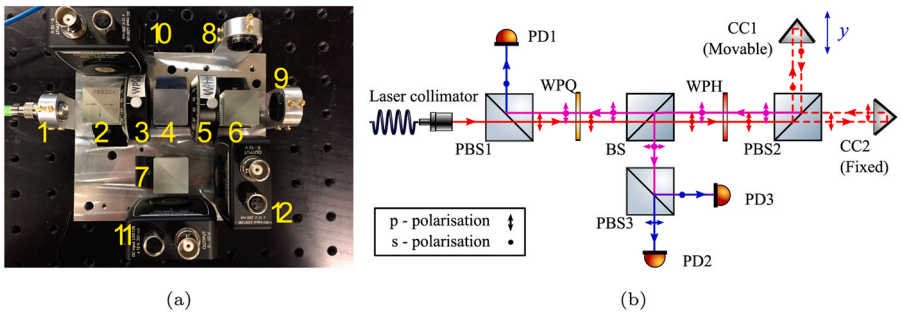

Fig. 7. The interferometric sensing part and its optical path: (a) The prototype of the interferometric readout: 1 laser collimator, 2&6&7 Polarising Beam Splitter Cubes (PBS1&2&3), 3 Quarter-Wave Plate (WPQ, 45° rotated), 4 Non-Polarising Beam Splitter Cube (BS), 5 Half-Wave Plate (WPH, 22.5° rotated), 8&9 Corner Cubes (CC1&2), 10&11&12 Switchable Gain Amplified Photodiodes (PD1&2&3); (b) Arrows indicate the direction of propagation. The red lines show single laser beams in different polarisation states, the solid purple lines represent the non-interfered recombined beams and the solid blue line shows the interfered recombined beams.

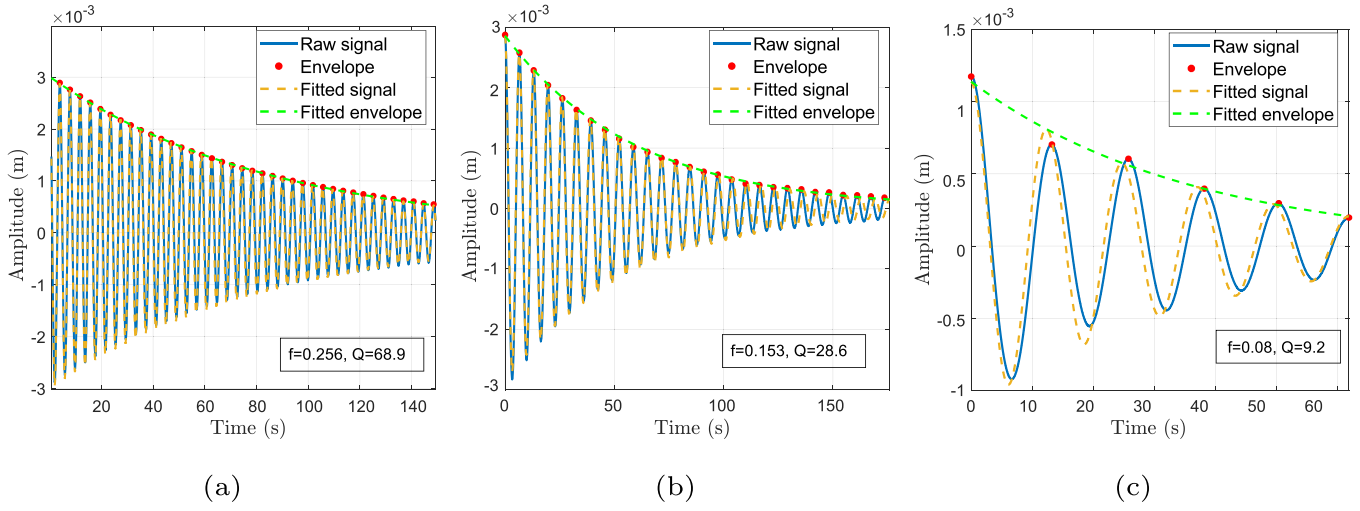

Fig. 8. The response of HINS to an impulse excitation (ring-down test) for different tilt angles: (a) − 1.5°, (b) 0° and (c) 0.6°.

wavelength of the laser beam in the vacuum and y is the physical optical path length that the beam travelled. Finally, the perfectly measured laser intensity in terms of the phase variation by the three photodetectors are

$$P_{\mathrm{PD1}} = \frac{1}{8}P_0()1 + \cos(2\phi_y)) \tag{15}$$

$$P_{\mathrm{PD2}} = \frac{1}{8}P_0()1 + \sin(2\phi_y)) \tag{16}$$

$$P_{\mathrm{PD3}} = \frac{1}{8}P_0()1 - \sin(2\phi_y)) \tag{17}$$

where, the coefficient 2 indicates the optical path is doubled by the reflector in the measurement arm.

By subtracting Eq. (17) from (15), and Eq. (16) from (15), the quadrature signals with respect to the sine and cosine function $Q_{\sin}$ and $Q_{\cos}$ are

$$Q_{\sin} = P_{\mathrm{PD1}} - P_{\mathrm{PD3}} = \frac{1}{8}P_0()1 + \cos(2\phi_y)) - \frac{1}{8}P_0()1 - \sin(2\phi_y))$$
$$= \frac{\sqrt{2}P_0}{8}\sin(2\phi_y + \frac{\pi}{4}) \tag{18}$$

$$Q_{\cos} = P_{\mathrm{PD1}} - P_{\mathrm{PD2}} = \frac{1}{8}P_0()1 + \cos(2\phi_y)) - \frac{1}{8}P_0()1 + \sin(2\phi_y))$$
$$= \frac{\sqrt{2}P_0}{8}\cos(2\phi_y + \frac{\pi}{4}) \tag{19}$$

where the DC offset $\frac{1}{8}P_0$ contains laser intensity noise is removed. However, A DC phase offset $\pi/4$ and the gain factor $\sqrt{2}$ are introduced from the subtraction. By using the arctan2 function with phase tracking, the measured phase $\hat{\phi}_y$ is extracted by

$$\hat{\phi}_y = \frac{\mathrm{arctan2}(Q_{\sin}, Q_{\cos}) - \frac{\pi}{4}}{2} \tag{20}$$

where the gain factor $\frac{\sqrt{2}P_0}{8}$ is cancelled out, and the item $-\pi/4$ on the right side compensates the DC phase offsets induced by subtractions (Eqs. (18) and (19)). According to Eqs. (14) and (20), the displacement of the movable corner cube is

$$\hat{y} = \frac{\lambda}{2\pi n}\cdot\hat{\phi}_y$$
$$= \frac{\lambda}{4\pi n}()\mathrm{arctan2}(Q_{\sin}, Q_{\cos}) - \frac{\pi}{4}) \tag{21}$$

where $\lambda = 1550$ nm is the wavelength of the laser beam and $n \simeq 1$ is the index of refraction. Eq. (21) indicates that the interferometric readout has an infinite measurement range.

In practice, the photodetectors outputs voltage signals in terms of the laser intensity, the uncertainties from the optoelectronic system, alignment, environment affects the quality of the signals. Therefore, the normalisation for removing unbalanced gains and offsets, and the ellipse fitting for correcting phase offsets are required [27,28] to treat raw voltage signals.

3. Experiments

In this section, experimental results are presented. A *dSpace MicroLabBox* system was used for the data acquisition. The whole control scheme was implemented in the *Matlab Simulink* environment and then downloaded to the processor unit of the *MicroLabBox* system. The control scheme was updated at a sampling frequency of 10 kHz, and the measured data was recorded at 1 kHz. The first set of experiments is to investigate the influence of the tilt angle to the characteristics of the HINS. Fig. 8a–8c plot the response of the HINS to a non-equilibrium initial excitation when the tilt angle is set to − 1.5°, 0° and 0.6°, respectively. The tilt angle is measured by a digital protractor (*Pro3600*) with a resolution of 0.01°. In order to extract the characteristics of the HINS, the following expression

$$y(t) = Ae^{-2\zeta\omega_0 t}\cos(\sqrt{1-4\zeta^2}\omega_0 t + \phi) \tag{22}$$

is used, which represents a classical solution of 1DOF system to an impulse excitation. $y(t)$ is the oscillation of the pendulum measured by the optical readout, A and ϕ are the initial gain and phase of the HINS, ω_0 and ζ are the natural frequency and the damping ratio.

The fitted results are superimposed in Fig. 12, based on which the resonance frequency and the Q factor of the HINS are extracted and summarised in Table 1.

As can be seen, the resonance frequency indeed decreases as the tilt angle decreases as theoretically predicted in Fig. 6. From the practical commissioning viewpoint, it is recommended not to set the tilt angle too low to avoid destabilizations of the system for example caused by the thermal variation.

The second set of experiments is conducted to study the steady response of the HINS. A test bench as shown in Fig. 9 is constructed which consists of an optical board (*MB6060/M*) sitting on two linear bearings (*LSP2080*). A piezo actuator (*APA100M*) is mounted on one end which is used to drive the optical board. An eddy-current sensor (*ECL101*) is mounted on the other end which picks up the relative

Table 1
Ring-down tests results.

Tilt angle (degree)	-1.5°	0°	0.6°
Resonance (Hz)	0.256	0.153	0.079
Quality factor	68.9	28.6	9.2

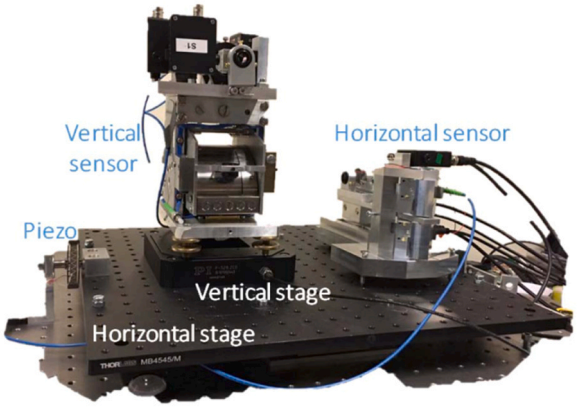

Fig. 9. Characterisation test bench.

motion of the optical board and the ground, denoted as x_0 hereafter. The HINS is mounted on the top of the board. Thus x_0 is considered as the base motion to the HINS. During the tests, a white noise signal was applied to drive the piezo actuator. The duration of the measurement was set to 2000s

The frequency response of the transfer function between the signals measured by the eddy-current sensor and the HINS is plotted in Fig. 10. It can be seen that the response at low frequency turns out to be a constant with respect to the excitation. In addition, the coherence also drops at low frequency. The reason behind is that some rotational excitations are generated in addition to the pure desired translation excitations when driving the piezo. The induced response to the rotational excitations actually dominates the low frequency response according to the analysis in Section 3. In order to verify this assumption, two displacement sensors (*Lion U8B* and *PI E-852*) are placed on the two ends of the optical board which measure the response of the board in the vertical direction. The vertical responses and its difference are shown in Fig. 10 when the piezo actuator is driven in the same condition as before. It can be seen that the difference is approximately a factor of two greater than the vertical response measured on either side which means that the board also undergoes a rotational motion. In Fig. 11, the responses when no excitations are injected are also superimposed in order to show the noise level of the sensor which is far lower than the measured signals. The injected horizontal and rotational motion are superimposed in Fig. 10, where the rotational motion is represented by the response difference in the vertical direction over a 45 cm span. Substituting the rotational and the translational excitations into Eq. (12), the response of the HINS for this particular set-up can be simulated. The simulation result is also plotted in Fig. 10, where a pair of real zeros (± 1.885) is obtained. Although the horizontal motion is two order of magnitude larger than the rotational motion, a strong tilt-horizontal coupling is observed. The results obtained during this study is interesting because it clearly illustrates how the rotational and translational excitations are coupled for the HINS. If the HINS is used as the feedback sensor for active seismic vibration isolation, attentions need to be paid on the location of the HINS such that the tilt-horizontal coupling occurs outside of the frequency band of interest and the resultant real zeros should be avoided for example by changing the orientation of the torque applied by the control actuator. From the control viewpoint, the system becomes a non-minimal phase system which makes it challenging to achieve a good vibration isolation performance.

4. Noise budgeting

The resolution of the HINS can be estimated by using the resolution of the interferometric readout multiplied by the inverse transmissibility T_{WY}^{-1} of the HINS (the inverse of T_{WY} in Eq. (6)). The resolution of the interferometric readout was estimated by the blocked-mass test, in which the two corner cubes on the interferometric readout are blocked. The Amplitude Spectral Density (ASD) of the measured readout resolution multiplied by T_{WY}^{-1} is shown by the solid blue curve. The theoretical readout noise contains noises originating from the data acquisition system, photodetectors, laser source and environment, among them the optoelectronic noise from the photodetectors is dominant. For comparison, the theoretical readout noise is multiplied by T_{WY}^{-1} (dash yellow curve) and shown in the figure. By comparing the measured resolution and the theoretical one, it shows that the measured readout resolution is limited by the optoelectronic noise of the readout from 0.01 to 1 Hz. Moreover, this readout is sensitive to the seismic vibration from 2 to 100 Hz. The reason is that the optical-component holders are not sufficiently rigid. Therefore, improving the rigidity of the structure is envisioned to better characterise the noise floor of the readout.

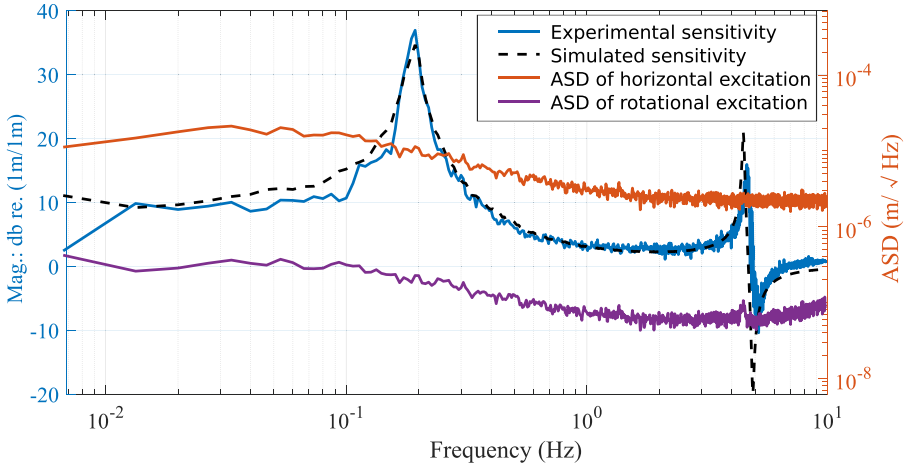

Fig. 10. Left axis: comparison of the transfer function between the eddy-current sensor and the HINS; Right axis: comparison of the horizontal and rotational motion when driving the piezo actuator.

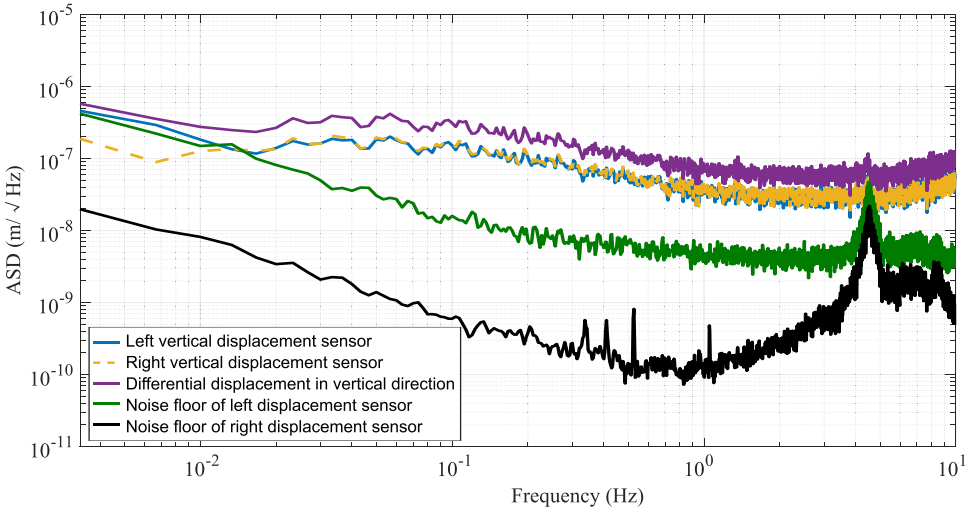

Fig. 11. ASD comparison of the response of the optical board in the vertical direction and the noise floor of the displacement sensors.

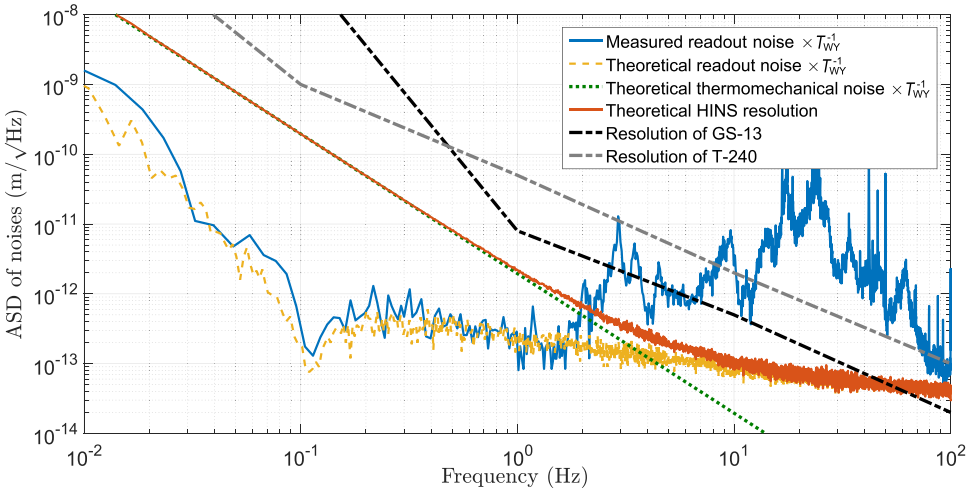

Fig. 12. Theoretical resolution of the HINS.

When the pendulum is free in measurements, thermomechanical noise (dash green curve) affects the mechanics. Thermomechanical noise n_{tm} is caused by the thermal fluctuation of the proof-mass. The ASD of the fluctuation is estimated by [29].

$$\mathrm{A_{ntm}} = \sqrt{\frac{4k_{\mathrm{B}}Tk/Q}{\omega[(k-m\omega^2)^2+k^2/Q^2]}} \quad (\mathrm{m}/\sqrt{\mathrm{Hz}}) \tag{23}$$

where $k_{\mathrm{B}} = 1.38064852 \times 10^{-23}$ J/K is the Boltzmann's constant and $T = 297.15$ K is the Kelvin temperature. According to the mechanical system of the HINS, the proof mass is $m = 0.5$ kg, the quality factor (Q factor) is $Q = 15$, the resonance frequency is $f_0 = 0.11$ Hz, the stiffness $k = m(2\pi f_0)^2 = 0.14$ N/m and the resonance $\omega_0 = 2\pi f_0 = 0.69$ rad can be found. The ASD of the theoretical thermomechanical noise multiplied by T_{WY}^{-1} (dash-dotted green curve) is shown in Fig. 8. It can be seen that it is higher than the optoelectronic noise from 0.01 to 1 Hz. Therefore, it dominates the resolution of HINS in the frequencies.

In conclusion, the theoretical resolution of the HINS (dash red curve) is obtained by adding the thermomechanical noise and interferometric readout noise. It is 2×10^{-13} m/$\sqrt{\mathrm{Hz}}$ at 1 Hz and is dominated by the thermomechanical noise from 0.01 to 1 Hz and by the optoelectronic noise from 1 to 100 Hz, and it outperforms than the resolution of outstanding commercial geophone, Geotech GS-13 (dash-dotted black curve), and the seismometer, Trillium T-240 (dash-dotted grey curve), in the market [6].

5. Conclusion

We have presented a novel interferometric inertial sensor for low-frequency active seismic isolation. Its mechanics consists of a pair of cross-spring hinges and an inverted-pendulum like structure, thanks to which the resonance frequency of the HINS can tuned. A dynamic analysis was performed which studies the sensitivities of the HINS to excitations in different directions. The readout of the HINS is a homodyne quadrature interferometer which allows to measure the relative displacement with a very high resolution and a large dynamic range. The theoretical analysis has also been experimentally validated. A ring-down test was performed which shows the resonance frequency of the HINS can reach as low as 0.08 Hz. The sensitivities of the HINS to transnational and rotational excitations have also been experimental examined which also backs up the theoretical analysis. A noise budgeting of HINS was given in the paper. It predicts that the resolution below 1 Hz is dominated by the thermomechanical noise and by unwanted internal vibrations of the interferometric readout between 1 Hz and 100 Hz. The future work will be focusing on suppressing the thermomechanical noise for example through lowering the surrounding temperature and the

vacuum level, and the internal vibrations through improving the rigidity of the mounting of the optical components.

CRediT authorship contribution statement

Binlei Ding: Conceptualization, Methodology, Experiment, Investigation, Validation, Writing – original draft preparation. **Guoying Zhao**: Experiment, Validation, Formal analysis, Writing – review & editing. **Jennifer Watchi**: Experiment, Writing – review & editing. **Ameer Sider**: Writing – review & editing. **Christophe Collette**: Supervision, Writing – review & editing.

Declaration of Competing Interest

The authors declare that they have no known competing financial interests or personal relationships that could have appeared to influence the work reported in this paper.

Acknowledgement

The authors gratefully acknowledge the CSC, China for funding Binlei Ding (grant number: 201607650017), the French Community as part of the financing of a FRIA grant for Jennifer Watchi (grant number: FC 27289), the FRS-FNRS (grant agreement: F.4536.17), National Key Research and Development Program of China (Grant No. 2020YFC2200701 and 2020YFC2200500) and the Innovation and Induction of Disciplines in Higher Education Institutions, China (grant agreement: 111 project B20062) for funding this research. Grateful thanks go to, dr. Michel Van Camp and his fellows from the Royal Observatory of Belgium and dr. Thomas Forbriger and ir. Edgar Wetzig from the Federal Institute for Geosciences and Natural Resources of Germany. They kindly lend us STS-1 seismometers which played a vital role in this project. We would especially thank the members of the LIGO Seismic Working Group for their comments and inspiring discussions, this paper can be found as LIGO-P2100210.

Appendix

Derivation of g_t

According to Fig. 3, defined in the Cartesian coordinate system, the unit vector $\mathbf{n_0} = [0, 0, 1]^\top$ presents the normal direction of the Ω plane. At the initial position shown in Fig. 3a, vectors $\mathbf{r_0} = [-1, 0, 0]^\top$ and $\mathbf{t_0} = [0, -1, 0]^\top$ present the radial and tangent directions of motion of the proof-mass. Fig. 3b presents the whole mechanics tilted about Y-axis with an angle γ_0. The Ω' plane (marked with red circle) presents the rotation plane of the proof-mass after tilting. Rotation matrices are used in the derivation, and they are given by [30].

$$R_x(\alpha) = \begin{bmatrix} 1 & 0 & 0 \\ 0 & \cos(\alpha) & \sin(\alpha) \\ 0 & -\sin(\alpha) & \cos(\alpha) \end{bmatrix}, R_y(\gamma) = \begin{bmatrix} \cos(\gamma) & 0 & -\sin(\gamma) \\ 0 & 1 & 0 \\ \sin(\gamma) & 0 & \cos(\gamma) \end{bmatrix}, R_z(\beta) = \begin{bmatrix} \cos(\beta) & \sin(\beta) & 0 \\ -\sin(\beta) & \cos(\beta) & 0 \\ 0 & 0 & 1 \end{bmatrix} \tag{24}$$

where $R_x(\alpha)$, $R_y(\gamma)$ and $R_z(\beta)$ are the rotation matrices of the proof-mass rotating about the point O. For space-fixed rotations, the normal vector $\mathbf{n_0}$ after tilting is

$$\mathbf{n_1} = R_y(\gamma_0)\cdot\mathbf{n_0} = [] - \sin(\gamma_0),\ 0,\ \cos(\gamma_0)]^\top \tag{25}$$

The radial vector $\mathbf{r_0}$ after tilting is

$$\mathbf{r_1} = R_y(\gamma_0)\cdot\mathbf{r_0} = [] - \cos(\gamma_0),\ 0,\ -\sin(\gamma_0)]^\top \tag{26}$$

The gravitational force of the proof-mass $\mathbf{G} = (0, 0, -mg)^\top$ has a projection on the vector $\mathbf{r_1}$ and it is

$$\begin{aligned} \mathbf{g_r} &= \mathbf{proj}_{\mathbf{r_1}}\mathbf{G} = \frac{\mathbf{r_1}\cdot\mathbf{G}}{\|\mathbf{r_1}\|^2}\cdot\mathbf{r_1} \\ &= -mg\sin(\gamma_0)\cdot[]\cos(\gamma_0),\ 0,\ \sin(\gamma_0)]^\top \end{aligned} \tag{27}$$

where, the vector $\mathbf{g_r}$ is the projection. $\mathbf{proj}_{\mathbf{r_1}}\mathbf{G}$ indicates the operation of projecting the vector $\mathbf{G}$ onto the vector $\mathbf{r_1}$, and $\|\mathbf{r_1}\|$ is the magnitude of the vector. The vector $\mathbf{g_r}$ points the rotation point in the Ω' plane, and its magnitude g_r is

$$g_r = \|\mathbf{g_r}\| = mg\sin(\gamma_0) \tag{28}$$

where g_r is the axial load applied on the joint. According to Eq. (1), the rotational stiffness of the joint can be estimated, and it is denoted by k_γ. The variation of the stiffness k_γ during oscillation is not addressed in the following discussion.

When the mechanics is tilted, the motion of the proof-mass causes the variation of potential energy. Therefore, the contribution of the gravitational force is taken into account. The tangent vector is used to find the component of the gravitational force in the Ω' plane. For space-fixed rotations, the tangent vector containing tilting angle γ_0 and rotation ω is

$$\mathbf{t_1} = R_y(\gamma_0)R_z(\omega)\cdot\mathbf{t_0} = -[]\sin(\omega)\cos(\gamma_0),\ \cos(\omega),\ \sin(\omega)\sin(\gamma_0)]^\top \tag{29}$$

The projection of the vector $\mathbf{G}$ on the vector $\mathbf{t_1}$ is

$$\begin{aligned} \mathbf{g_t} &= \mathbf{proj}_{\mathbf{t_1}}\mathbf{G} = \frac{\mathbf{t_1}\cdot\mathbf{G}}{\|\mathbf{t_1}\|^2}\cdot\mathbf{t_1} \\ &= -mg\sin(\gamma_0)\sin(\omega)\cdot[]\sin(\omega)\cos(\gamma_0),\ \cos(\omega),\ \sin(\omega)\sin(\gamma_0)]^\top \end{aligned} \tag{30}$$

where $\mathbf{g_t}$ is the component of the gravitational force in the Ω' plane and its magnitude g_t is

$$g_t = \|\mathbf{g_t}\| = mg\sin(\gamma_0)\sin(\omega) \tag{31}$$

Derivation of the β_n and the related g_t

As shown in Fig. 4b, the scalar projection of the vector $\boldsymbol{\beta} = [0, \beta, 0]^\top$ on the Ω' plane is given by

$$\beta_n = \|\mathbf{proj}_{\mathbf{n_1}}\boldsymbol{\beta}\| = \|\frac{\mathbf{n_1}}{\cdot}\boldsymbol{\beta}\|\mathbf{n_1}\|^2 \cdot \mathbf{n_1}\| = \beta\cos(\gamma_0) \tag{32}$$

where β_n denotes the counter-clockwise rotation of the frame in the Ω' plane. Because both of the frame and the proof-mass rotates in the Ω' plane. The relationship between rotations is

$$\omega = \theta - \beta\cos(\gamma_0) \tag{33}$$

where ω is the rotation of the proof-mass and θ is the relative angle between the frame and the proof-mass. Therefore, combining Eq. (33), the magnitude of the vector $\mathbf{g_t}$ is

$$g_t = \|\mathbf{g_t}\| = mg\sin(\gamma_0)\sin()\theta - \beta\cos(\gamma_0)) \tag{34}$$

Derivation the α_n and related g_t

According to Fig. 4c, the mechanics is under the excitation of $\boldsymbol{\alpha} = [\alpha, 0, 0]^\top$ about X-axis. The scale of the excitation on the Ω' plane is

$$\alpha_n = \|\mathbf{proj}_{\mathbf{n_1}}\boldsymbol{\alpha}\| = \|\frac{\mathbf{n_1}\cdot\boldsymbol{\alpha}}{\|\mathbf{n_1}\|^2}\cdot\mathbf{n_1}\| = -\alpha\sin(\gamma_0) \tag{35}$$

where the minus symbol denotes the clockwise rotation of the frame in the Ω' plane. In this case, the ω in Eq. (31) is

$$\omega = \theta + \alpha\sin(\gamma_0) \tag{36}$$

Because the mechanics tilts about X-axis, the gravitational force plays a role here for influencing the dynamics of the HINS. For space-fixed rotations, the tangent vector $\mathbf{t_1}$ is

$$\mathbf{t_1} = R_y(\gamma_0)R_z(\alpha)R_z(\omega)\cdot\mathbf{t_0} = -\begin{bmatrix}\sin(\omega)\cos(\gamma_0) + \cos(\omega)\sin(\gamma_0)\sin(\alpha)\\ \cos(\omega)\cos(\gamma_0)\\ \sin(\omega)\sin(\gamma_0) - \cos(\gamma_0)\sin(\alpha)\cos(\omega)\end{bmatrix} \tag{37}$$

The vector $\mathbf{G}$ has a projection $\mathbf{g_t}$ on the vector $\mathbf{t_1}$. Combining with Eq. (36), the scalar of the projected vector is

$$g_t = \|\mathbf{g_t}\| = \|\mathbf{proj}_{\mathbf{t_1}}\mathbf{G}\| = mg(\sin(\omega)\sin(\gamma_0) - \cos(\gamma_0)\sin(\alpha)\cos(\omega))) \tag{38}$$

References

[1] G.M. Harry, L.S. Collaboration, et al., Advanced LIGO: the next generation of gravitational wave detectors, Class. Quantum Gravity 27 (8) (2010) 084006.
[2] K. Artoos, C. Collette, M. Guinchard, M. Sylte, B. Bolzon, O. Capatina, A. Jeremie, C. Hauviller, Ground vibration and coherence length measurements forthe CLIC nano-stabilization studies (CERN-ATS-2009-126. CLIC-Note-795) 3.
[3] C. Collette, S. Janssens, P. Fernandez-Carmona, K. Artoos, M. Guinchard, C. Hauviller, A. Preumont, Inertial sensors for low-frequency seismic vibration measurement, Bull. Seismol. Soc. Am. 102 (4) (2012) 1289–1300.
[4] C. Collette, S. Janssens, K. Artoos, Review of active vibration isolation strategies, Recent Patents Mech. Eng. 4 (3) (2011) 212–219.
[5] F. Matichard, B. Lantz, R. Mittleman, K. Mason, J. Kissel, B. Abbott, S. Biscans, J. McIver, R. Abbott, S. Abbott, et al., Seismic isolation of advanced LIGO: review of strategy, instrumentation and performance, Class. Quantum Gravity 32 (18) (2015) 185003.
[6] B. Lantz, J. Kissel, Sensor noise estimates for advanced LIGO seismic isolation systems, Tech. Note LIGO-T900450, LIGO at Stanford, United States (Feb., 2017).
[7] Geotech, Short-period Seismometer: Model S-13 and GS-13, DS-18300, Geotech Instruments, LLC., United States. ⟨http://www.geoinstr.com/ds-s13.pdf⟩.
[8] LIGO Scientific Collaboration, Instrument science whitepaper 2019, Tech. Note LIGO-T1900409, SLAC National Accelerator Lab., Menlo Park, CA (United States) (Nov., 2019).
[9] M. Pisani, A homodyne michelson interferometer with sub-picometer resolution, Meas. Sci. Technol. 20 (8) (2009) 084008.
[10] J. Watchi, S. Cooper, B. Ding, C.M. Mow-Lowry, C. Collette, Contributed review: a review of compact interferometers, Rev. Sci. Instrum. 89 (12) (2018) 121501.
[11] M. Zumberge, J. Berger, J. Otero, E. Wielandt, An optical seismometer without force feedback, Bull. Seismol. Soc. Am. 100 (2) (2010) 598–605.
[12] B. Ding, Development of High Resolution Interferometric Inertial Sensors (Ph.D. Thesis), Université libre de Bruxelles, Brussels, 2021.
[13] S.J. Cooper, Breaking the sEismic Wall: How to Improve Gravitational Wave Detectors at Low Frequency (Ph.D. Thesis), University of Birmingham, Birmingham, 2020.
[14] C. Collette, F. Nassif, J. Amar, C. Depouhon, S.-P. Gorza, Prototype of interferometric absolute motion sensor, Sens. Actuators A Phys. 224 (2015) 72–77.
[15] M. Pisani, M. Zucco, An accelerometer for spaceborne application with interferometric readout, Measurement 122 (2018) 507–512.
[16] A. Bertolini, N. Beverini, G. Cella, R. DeSalvo, F. Fidecaro, M. Francesconi, D. Simonetti, Geometric anti-spring vertical accelerometers for seismic monitoring, Nucl. Instrum. Methods Phys. Res. Sec. A Accel. Spectrom. Detect. Assoc. Equip. 518 (1–2) (2004) 233–235.
[17] A. Hines, L. Richardson, H. Wisniewski, F. Guzman, Optomechanical inertial sensors, Appl. Opt. 59 (22) (2020) G167, https://doi.org/10.1364/ao.393061
[18] A. Bertolini, R. DeSalvo, F. Fidecaro, A. Takamori, Monolithic folded pendulum accelerometers for seismic monitoring and active isolation systems, IEEE Trans. Geosci. Remote Sens. 44 (2) (2006) 273–276.
[19] F. Acernese, R. De Rosa, G. Giordano, R. Romano, S. Vilasi, F. Barone, Low frequency-high sensitivity horizontal inertial sensor based on folded pendulum, Journal of Physics: Conference Series vol. 363, IOP Publishing, 2012012001.
[20] F. Barone, G. Giordano, The UNISA folded pendulum: a very versatile class of low frequency high sensitive sensors, Measurement 118 (2018) 339–347.
[21] J.V. van Heijningen, A fifty-fold improvement of thermal noise limited inertial sensitivity by operating at cryogenic temperatures, J. Instrum. 15 (06) (2020) P06034.
[22] Streckeisen, Very-broad-band Feedback Seismometers, STS-1V/VBB and STS-1H/VBB, STS1-VBB, Rev. 1, G Streckeisen AG, Switzerland. URL ⟨http://www.software-for-seismometry.de/textfiles/Seismometry/STS-1_datasheet.pdf⟩.
[23] H. Zhao, S. Bi, Stiffness and stress characteristics of the generalized cross-spring pivot, Mech. Mach. Theory 45 (3) (2010) 378–391.
[24] E. Wielandt, P. Bormann, Seismic sensors and their calibration, New Man. Seismol. Obs. Pract. 1 (2002) 46.
[25] J. Liu, R. Azzam, Polarization properties of corner-cube retroreflectors: theory and experiment, Appl. Opt. 36 (7) (1997) 1553–1559.
[26] J.D. Ellis, Field Guide to Displacement Measuring Interferometry, SPIE Press, Washington USA, 2013.
[27] P.L. Rosin, A note on the least squares fitting of ellipses, Pattern Recognit. Lett. 14 (10) (1993) 799–808.
[28] T. Požar, J. Možina, Enhanced ellipse fitting in a two-detector homodyne quadrature laser interferometer, Meas. Sci. Technol. 22 (8) (2011) 085301.

[29] P.R. Saulson, Thermal noise in mechanical experiments, Phys. Rev. D 42 (8) (1990) 2437.
[30] J.H. Ginsberg, Advanced Engineering Dynamics, Cambridge University Press, 1998.

Binlei Ding received the M.Sc. and Ph.D. degrees from Université Libre de Bruxelles, Belgium, in 2016 and 2021, respectively. Since 2021, he has been a Senior Electronics Engineer with BYD, Shenzhen, China. His current research interests include high-precision instruments, optical positioning systems, high-performance sensors, sensor interface electronics and data processing.

Guoying Zhao received Ph.D. degree from KU Leuven, Belgium, in 2015. He is currently an associate professor at Sun Yat-Sen University, China. His main research interests include active and passive control of vibration, inertial sensors and actuators, and gravitational wave detectors.

Jennifer Watchi received her bachelor's degree in engineering physics and her master's degree in engineering physics, specializing in applied physics, from the Université Libre de Bruxelles in 2013 and 2015. Since 2015, she has been a doctoral candidate at the Precision Mechatronics Laboratory.

Ameer Sider received his bachelor degree in Mechatronics engineering (honoured) at International Islamic University Malaysia (IIUM) in 2012 and received M.Sc. in Control System and Automation Engineering from University of Putra Malaysia (UPM) in 2014. Currently, Mr Sider is a PhD student at University of Liège, Belgium, and is working on the active control of vibration.

Christophe Collette received an M.Sc. in physics engineering from the University of Liège in 2001 and Ph.D. degree in mechatronics engineering from the Université Libre de Bruxelles in 2007. He is currently a full professor at University of Liège and director of the Precision Mechatronics Laboratory. His main research interests include the active and passive control of vibration, optical inertial sensors and future space telescopes.